Monthly Notices
of the
ROYAL ASTRONOMICAL SOCIETY

MNRAS **465,** 4482–4499 (2017) doi:10.1093/mnras/stw2931

Do water fountain jets really indicate the onset of the morphological metamorphosis of circumstellar envelopes?

Bosco H. K. Yung,[1,2]★ Jun-ichi Nakashima,[3,2] Chih-Hao Hsia[5,4,2] and Hiroshi Imai[6]

[1]*Nicolaus Copernicus Astronomical Center, Rabiańka 8, PL-87-100 Toruń, Poland*
[2]*Department of Physics, The University of Hong Kong, Pokfulam Road, Hong Kong*
[3]*Department of Astronomy and Geodesy, Ural Federal University, Lenin Ave. 51, 620000 Ekaterinburg, Russia*
[4]*Laboratory for Space Research, Faculty of Science, The University of Hong Kong, Pokfulam, Hong Kong*
[5]*Space Science Insitute, Macau University of Science and Technology, Avenida Wai Long, Taipa, Macau*
[6]*Graduate School of Science and Engineering, Kagoshima University, 1-21-35 Korimoto, 890-0065 Kagoshima, Japan*

Accepted 2016 November 10. Received 2016 November 10; in original form 2016 June 7

ABSTRACT

Small-scale bipolar jets with short dynamical ages from 'water-fountain' (WF) sources are regarded as an indication of the onset of circumstellar envelope morphological metamorphosis of intermediate-mass stars. Such a process usually happens at the end of the asymptotic giant branch (AGB) phase. However, recent studies found that WFs could be AGB stars or even early planetary nebulae. This fact prompted the idea that WFs may not necessarily be objects at the beginning of the morphological transition process. In the present work, we show that WFs could have different envelope morphologies by studying their spectral energy distribution profiles. Some WFs have spherical envelopes that resemble usual AGB stars, while others have aspherical envelopes, which are more common to post-AGB stars. The results imply that WFs may not represent the earliest stage of morphological metamorphosis. We argue further that the dynamical age of a WF jet, which can be calculated from maser proper motions, may not be the real age of the jet. The dynamical age cannot be used to justify the moment when the envelope begins to become aspherical, nor to tell the concrete evolutionary status of the object. A WF jet could be the innermost part of a larger well-developed jet, which is not necessarily a young jet.

Key words: radiative transfer – stars: AGB and post-AGB – stars: evolution – stars: mass-loss – stars: winds, outflows – infrared: stars.

1 INTRODUCTION

Planetary nebulae (PNe) that evolved from stars with masses about 1–8 $M_{\odot}$ have different morphologies, such as spherical, bipolar or even multipolar (see Kwok 2010 for a review). In contrast, their progenitors, mass-losing asymptotic giant branch (AGB) stars, are mostly just spherical in terms of their circumstellar envelopes (or envelopes). A vast change in morphology is expected to have happened in between the AGB and PN phases, called the post-AGB phase. It is suggested that high-velocity jets emerging from late/post-AGB stars play a key role in shaping PNe (Sahai & Trauger 1998; Sahai & Patel 2015). Nonetheless, the exact jet formation mechanism and the jet–envelope interaction process are still unclear. While larger bipolar structures likely resulting from jets can be observed in infrared or optical images (e.g. Sahai, Morris & Claussen 2007; Siódmiak et al. 2008; Lagadec et al. 2011), some jets can only be revealed by interferometric observation of molecular lines such as CO. The spatial extent of such molecular jets could reach a few thousand au from the star: e.g. ∼6000 au for the post-AGB star IRAS 08005−2356 (Sahai & Patel 2015), with velocity >100 km s^{-1}. Some molecular outflows (jets or tori) have also been observed occasionally in AGB stars, e.g. V Hydrae (Hirano et al. 2004) and X Herculis (Nakashima 2005).

In the case of oxygen-rich stars, which are evolved stars with more oxygen than carbon in the envelopes, types of object called 'water fountains' (WFs) exist, which have relatively 'tiny' collimated jets traced by 22-GHz H_2O maser emission (see Imai 2007; Desmurs 2012, for reviews on WFs). The spatial extent of WF jets is usually relatively small, of order 10^2–10^3 au (e.g. Imai et al. 2002; Boboltz & Marvel 2007; Day et al. 2010; Yung et al. 2011). These jets are characterized by the large spectral velocity coverage (usually >50 km s^{-1}) of H_2O maser emission, which exceeds the usual 1612-MHz OH maser coverage (≤25 km s^{-1}: te Lintel Hekkert et al. 1989). WFs are relatively rare, as there are only 16 confirmed examples known to date plus a few candidates reported in Yung

★ E-mail: byung@ncac.torun.pl

et al. (2013), Yung, Nakashima & Henkel (2014) and Gómez et al. (2015a). There are several possible reasons why they might be rare. Gómez et al. (2015a) suggest that the WF phenomenon may in fact not be that uncommon, but the maser emission from most such objects is too weak to be detected; the exact mechanism is unknown, but it could be related to the masses of the star progenitors. Another reason is related to the viewing angle to the jet, as explored in Yung et al. (2013): even if the jet velocity is high, when the jet orientation is rather edge-on, the H_2O maser velocity coverage may still be smaller than that of the corresponding OH maser due to projection. Chemical bias could also be a reason, because we are focusing only on oxygen-rich stars and there is currently no way to observe WF equivalence for carbon-rich stars.

The dynamical ages of WF jets are found to be very short ($\leq$100 yr: Imai 2007). Together with the small jet sizes, most of the WFs are thought to be objects at the beginning stage of the morphological transition, which usually happens in the early post-AGB phase (e.g. Suárez, Gómez & Miranda 2008; Walsh et al. 2009; Day et al. 2010; Desmurs 2012). However, even though the majority of the WFs are very likely to be post-AGB stars, e.g. IRAS 16342−3814 (Sahai et al. 1999), IRAS 18113−2503 (Gómez et al. 2011), IRAS 18286−0959 (Yung et al. 2011) and IRAS 18455+0448 (Vlemmings et al. 2014), there are some clear exceptions. W43A shows flux variation in the OH maser with a period of 400 d, which is caused by a periodic variation in infrared emission due to envelope pulsation (Herman & Habing 1985; Imai et al. 2002). The SiO maser is also detected towards this object (Nakashima & Deguchi 2003). These indicate that W43A might still be in the AGB phase. On the other hand, IRAS 15103−5754 is suggested to be a PN candidate but also exhibits WF characteristics (i.e. high-velocity H_2O maser emission). Detection of the Ne II emission line and free–free continuum emission gives evidence of the PN status, making this object the first WF–PN ever found (Suárez et al. 2009; Lagadec et al. 2011; Gómez et al. 2015b). Given the above exceptions, it is suspected that WF-type objects are not necessarily in the short early post-AGB phase or transitional phase. They also may not represent the onset of morphological metamorphosis of AGB envelopes. Furthermore, the relationship between WF maser jets, larger-scale molecular jets and the ultimate large bipolar feature visible in the infrared is not known.

To find out the role of WF jets in such a morphological change process, one option is to examine whether there is a direct correlation between WF jets and the envelope morphology of WF sources. This can be done by looking at the infrared spectral energy distributions (SEDs). This is because the SED profile can give constraints on the possible envelope morphology of an AGB/post-AGB star. In this article, SEDs of known WFs are presented, together with dust radiative transfer models. However, the main goal here is to explore whether the dust envelopes of WFs have departed from spherical symmetry, not the deep interpretation of model parameters. Some of the WFs are shown to have aspherical structures under high-resolution infrared images (e.g. Lagadec et al. 2011; Ramos-Larios et al. 2012); nonetheless, a number of them may still have spherical envelopes. This work is also the first attempt to study WF envelopes collectively by radiative transfer models. This simple but effective approach will be useful in the future for statistical studies of stellar maser sources, which will be detected with new telescopes such as the Square Kilometre Array (SKA) and Five hundred metre Aperture Spherical Telescope (FAST). The amount of data resulting from these anticipated maser surveys will be huge and hence developing quick analysis approaches is very meaningful.

The data and SED analysis are described in Section 2. The results and interpretations are given in Section 3, followed by a discussion in Section 4. Finally, our conclusions are presented in Section 5.

2 SED ANALYSIS

2.1 Method

PNe are visible in the optical and hence morphological classification can be made from optical images (e.g. Ueta, Meixner & Bobrowsky 2000). In contrast, AGB and some post-AGB stars are optically opaque due to their thick envelopes and the detailed envelope structures are mostly visible in infrared wavelengths. Therefore, in this study we focus on the infrared SED data. The main concern here is whether WFs have spherical or aspherical (infrared) envelopes, hence a one-dimensional radiative transfer code is chosen for this analysis. However, this is not a very 'standard' radiative transfer analysis. In our case, the parameters obtained are not our greatest interest; instead, we focus on whether the SED profiles can be fit by the models.

The SED of an AGB/post-AGB star with clear aspherical envelope is unlikely to be reproduced by one-dimensional models. However, to confirm whether there is really no good fit for an SED is not so straightforward. This is because the SED profile shape is affected not only by the envelope morphology but also by the stellar temperature, chemistry and the number of dust components, etc. In order to be sure that a certain SED cannot be fitted, in principle we have to explore all physically possible combinations of parameters. Nonetheless, this is not feasible in practice, therefore specific cases will be examined to help exclude some less sensitive parameters (more in Section 2.3). After that, we can be more confident that the 'unfit' SEDs are associated with aspherical envelope morphology, but not due to other parameters. If WFs can have both spherical and aspherical envelopes, then it means that not all of them are at the same (early) stage of the morphology-changing process.

To justify the effectiveness of this fitting method, six standard AGB stars and six characteristic post-AGB stars were also included in our sample as a control for comparison (more in Section 2.4). The majority of AGB stars are expected to have spherical envelopes, but there are also a few clear exceptions, due to the existence of (early) jets, such as V Hydrae (Hirano et al. 2004), X Herculis (Nakashima 2005) and CIT 6 (e.g. Monnier, Tuthill & Danchi 2000). Aspherical features are more commonly found in post-AGB stars. It is expected that good SED fits can be obtained from the one-dimensional code for most of the spherical AGB stars, but not always for post-AGB stars (more in Section 2.4). We believe that if some meticulous manipulation is performed on the parametric values, it might be possible to fit SEDs of aspherical objects even with one-dimensional models, but this does not mean the solution is really physical. We try to avoid such over-manipulation by limiting our fitting using three defining parameters.

2.2 Data retrieved

The research targets include 17 objects. They are either known WFs in which the existence of bipolar jets has been confirmed by interferometric observations or WF candidates with possible AGB/post-AGB evolutionary status that show WF spectral characteristics in single-dish observations (i.e. velocity coverage of the H_2O maser is larger than that of the OH maser). In this article, these objects are all treated as 'WFs'. The object list, with corresponding references, is given in Table 1.

Table 1. List of objects studied. See text for details of the DUSTY fit. Envelope morphological information obtained from images, if any, is given in the 'Image' column. For water fountains and candidates, the representative articles discussing maser kinematics and evolutionary statuses are given in the last column.

Object	RA (J2000.0)	Dec. (J2000.0)	Image[a]	DUSTY[b]	WF Ref.
		Water fountains			
IRAS 15445−5449	15 48 19.37	−54 58 21.2	As	···	Pérez-Sánchez et al. (2011)
IRAS 15544−5332	15 58 18.40	−53 40 40.0	···	···	Deacon et al. (2007)
IRAS 16342−3814	16 37 39.91	−38 20 17.3	As	ND	Sahai et al. (1999)
IRAS 16552−3050	16 58 27.80	−30 55 06.2	···	NE	Suárez et al. (2008)
IRAS 18043−2116	18 07 21.10	−21 16 14.2	Un	···	Walsh et al. (2009)
IRAS 18056−1514	18 08 28.40	−15 13 30.0	···	ND	Yung et al. (2013)
IRAS 18113−2503	18 14 27.26	−25 03 00.4	···	D?	Gómez et al. (2011)
OH 12.8−0.9	18 16 49.23	−18 15 01.8	Un	S	Boboltz & Marvel (2007)
IRAS 18286−0959	18 31 22.93	−09 57 21.7	Un	···	Yung et al. (2011)
OH 16.3−3.0	18 31 31.51	−16 08 46.5	···	NE	Yung et al. (2014)
W 43A	18 47 41.16	−01 45 11.5	As	ND	Imai et al. (2002)
IRAS 18455+0448	18 48 02.30	+04 51 30.5	···	S	Vlemmings et al. (2014)
IRAS 18460−0151	18 48 42.80	−01 48 40.0	Un	ND	Imai et al. (2013b)
IRAS 18596+0315	19 02 06.28	+03 20 16.3	···	NE	Amiri et al. (2011)
IRAS 19134+2131	19 15 35.22	+21 36 33.9	Un	ND	Imai et al. (2007)
IRAS 19190+1102	19 21 25.09	+11 08 41.0	···	ND	Day et al. (2010)
IRAS 19356+0754	19 38 01.90	+08 01 32.0	···	D	Yung et al. (2014)
		Control AGB stars			
IRAS 14247+0454	14 27 16.39	+04 40 41.1	···	S	···
IRAS 18556+0811	18 58 04.23	+08 15 30.8	···	S	···
IRAS 19149+1638	19 17 11.55	+16 43 54.5	···	S	···
IRAS 19312+1130	19 33 34.56	+11 37 02.6	···	S	···
IRAS 19395+1827	19 41 44.55	+18 34 25.8	···	S	···
IRAS 19495+0835	19 51 57.71	+08 42 54.6	···	S	···
		Control post-AGB stars			
IRAS 07134+1005	07 16 10.26	+09 59 48.0	As	···	···
OH 231.8+4.2	07 42 16.95	−14 42 50.2	As	···	···
IRAS 17441−2441	17 47 13.49	−24 12 51.4	As	ND	···
IRAS 17534+2603	17 55 25.19	+26 02 60.0	Un	S?	···
IRAS 20547+0247	20 57 16.28	+02 58 44.6	Un	S?	···
IRAS22272+5435	22 29 10.37	+54 51 06.4	As	D	···

Notes. [a]Images are taken from Lagadec et al. (2011) or from the WF reference articles. Envelopes showing extended aspherical features are denoted by 'As', unresolved envelopes are denoted by 'Un'.
[b]SED profiles that can be fitted by DUSTY models are classified into single-peaked 'S' or double-peaked 'D'. The extra '?' indicates that the SEDs are marginally fitted by the models. For the profiles that cannot be fitted, many belong to two categories: those with near-infrared excess 'NE' compared with the models and those with near-infrared deficit 'ND'. See Section 3.1 for details.

The infrared photometric data (from 1.25–160 μm) used to construct the SEDs were collected from the point-source catalogues of the *Two Micron All Sky Survey* (*2MASS*: Skrutskie et al. 2006), *Wide-field Infrared Survey Explorer* (*WISE*: Wright et al. 2010), *Infrared Astronomical Satellite* (*IRAS*: Neugebauer et al. 1984), *Midcourse Space Experiment* (*MSX*: Egan et al. 2003) and *AKARI* (Kataza et al. 2010; Yamamura et al. 2010). More data were obtained from the images taken by the Infrared Array Camera (IRAC: Fazio et al. 2004) and the Multiband Imaging Photometer for *Spitzer* (*MIPS*: Rieke et al. 2004) mounted on the *Spitzer Space Telescope*. The method of performing photometry on these images is described in Hsia & Zhang (2014). All the above data are presented in Appendix A.

For W43A, we have additional submillimetre flux data obtained by the Very Large Array (VLA): 4.02 mJy at 7 mm (Imai et al. 2005), new observation results from the Berkeley Illinois Maryland Association (BIMA) Millimeter Array, Nobeyama Millimetre Array (NMA) and the Jansky–Very Large Array (JVLA, an upgraded version of the original VLA) covering wavelengths from about 1.3–30 mm. The BIMA observations (project code: t817d229) were conducted on 2003 September 7 and 12 with the D array. Uranus and MWC 349 were used as flux calibrators and 1751+096 as a phase calibrator. Calibration and image synthesis were performed with MIRIAD.[1] The flux obtained was 250 mJy at 1.3 mm with a root-mean-square (rms) noise of about 26.8 mJy per beam. The NMA observations were carried out on 2002 December 25–26 with the D configuration, 2003 January 10–11 with the AB configuration and 2003 March 27–28 with the C configuration. The JVLA observations (project code: 13A–041) were carried out on 2013 June 9 with the *Q* band (46.0 GHz), 2013 June 12 with the *X* band (10.1 GHz) and 2013 June 13 with the *K* band (24.2 GHz). J184603.8−000338 was used as the phase calibrator for the *X* and *K* bands and J185146.7+003532 for the *Q* band. OT081 was used as the bandpass and flux calibrator for the *K* and *Q* bands and 3C286 for the *X* band. Calibration and image synthesis of the NMA data

[1] https://bima.astro.umd.edu/miriad/

were performed with AIPS,[2] while for the JVLA data CASA[3] was used to produce image cubes which were then analysed with AIPS. Details of the NMA and JVLA observation results are given in Table A7.

We understand that other photometric/spectral data may exist for some of the objects; however, the above data are sufficient to construct unambiguous SEDs, which is good enough for our scientific purpose. Our focus is on the general profile shape of the SEDs, but not the detailed chemistry of the line features. The effects of interstellar extinction are known to be significant, especially towards the direction near to the Galactic plane and bulge. Such effects are prominent for shorter wavelengths. Thus, for data with wavelengths shorter than 8 μm, correction for interstellar extinction is necessary. The method used is described in Howarth (1983) and the required extinction coefficient for each object was determined from the Galactic reddening maps given by Schlegel, Finkbeiner & Davis (1998) and Schlafly & Finkbeiner (2011). The extinction values $A(V)$ are listed in Table A1.

2.3 One-dimensional radiative transfer modelling

The one-dimensional dust radiative transfer models used to fit the SEDs were generated by the DUSTY code (Ivezić, Nenkova & Elitzur 1999). As mentioned before, even though it is not possible to consider all combinations of different parameters, we tried to justify the most important ones for our purpose by performing specific tests. At the end we are left with three running parameters (see below).

We assumed that the radiation was coming from a point-source in the centre of the spherical envelope. The SEDs from the central point sources were taken to be Planckian (i.e. blackbody curves). We once thought that ultraviolet (UV) emission was detected from two of our WFs (IRAS 16552−3050 and OH 16.3−3.0) when we were searching through the source catalogue[4] of the *Galaxy Evolution Explorer* (*GALEX*). The UV emission might in principle be coming from e.g. a hot binary component, such as a white dwarf, and such binary systems are not rare. However, it is now confirmed that the UV detections are not associated with our two WFs, because the separations are too large (>0.5 arcmin) and other sources exist that are more likely to be hosts of the UV emission. The detected UV fluxes also seem to be unreasonably large if we assume the typical case of a binary including a white dwarf. No other obvious sign of binary components was observed from our samples according to our data, hence the single point-source model remains more reasonable. Note that we are not excluding binary cases here, but with our current data we do not intend to overinterpret this idea. Some possible cases with hot companions are mentioned in Sections 3 and 4.

A grain type with 50 per cent warm (Sil–Wc) and 50 per cent cold (Sil–Oc) silicates was chosen (Ossenkopf, Henning & Mathis 1992). While AGB stars consist of envelopes with warmer dust, the detached envelopes of post-AGB stars would have colder dust. Since we were uncertain about the exact situation for each case, we took the 50/50 assumption. In fact, we have tested that, within our temperature ranges (see Table 2), this warm–cold ratio has minimal effect on the SED profile shape. More warm dust would shift the model curve up in the mid-infrared by less than a few per cent, but still keep the curve shape quite precisely. We judge that this small shift does not affect our results much, because once again our main goal is not to determine the physical conditions of the dust envelopes very accurately but rather to see whether obtaining a reasonably good fit is possible or not. The grain size distribution was set to follow the standard Mathis–Rumpl–Nordsieck (MRN: Mathis, Rumpl & Nordsieck 1977) power law. Regarding the analytical profiles, we selected the DUSTY option, which supposed the envelope expansion was driven by radiation pressure on the dust grains. This was suitable for the case of mass-losing stars. The analytic approximation for radiatively driven winds was used, where the variation of flux-averaged opacity with radial distance was assumed to be negligible, so that the hydrodynamics equations could be solved analytically. This approximation offered the advantage of a much shorter run time and was suggested to be suitable for most AGB stars (Ivezić et al. 1999). The envelope thickness was assumed to be 10 000 times its inner radius. We also tested that even changing this ratio up to 40 per cent would have a negligible change on our model curves.

Table 2. Ranges and steps of the parameters used in generating the DUSTY models.

Parameter	Range	Step
$T_{\rm eff}$ (K)	1600–10000	200
$T_{\rm d}$ (K)	100–1600	100
$\tau_{2.2}$	0.01–0.1	0.005
$\tau_{2.2}$	0.11–0.3	0.01
$\tau_{2.2}$	0.35–0.95	0.05
$\tau_{2.2}$	1–10	1

Three running parameters remained for the DUSTY code under the above considerations, namely the effective temperature of the central radiation source ($T_{\rm eff}$), the dust temperature at the inner envelope boundary ($T_{\rm d}$) and the optical depth at 2.2 μm ($\tau_{2.2}$). To find the best-fitting models for the SEDs, we generated a model grid with all combinations of the three parameters within defined numerical ranges. The setting of the ranges and steps for each parameter is given in Table 2. The closest fit was obtained by minimizing the sum of squares of the flux deviations between the observed data points and the model curves (with appropriate scaling). Generally speaking, in our case the good fits are those that have the lowest sum-of-square values, $\sim 10^{-13}$. Note that in some marginal fit cases, or when multiple fit solutions seem plausible, the best fits finally have to be determined qualitatively by eye. For instance, we have to see whether the model can reproduce the key features of an SED line shape, such as the number of peaks and general changes of slopes. Even when the data points are a bit off from the model curve, it could still be considered as a good fit if the above general important features are reproduced. These cases will be discussed in Section 3.

2.4 Justification with control objects

Some control objects were used to test whether the DUSTY models were sensitive enough to distinguish spherical and aspherical envelopes. We mainly selected AGB and post-AGB stars with known envelope morphologies (e.g. from high-resolution infrared images) and, reasonably, enough photometric data points for SED construction. These objects were found in roughly the same RA range as the WFs, so as to minimize the effect of any possible position-dependent factors, e.g. to avoid huge differences in the galactic dust extinction towards the sources. Such extinction will affect the SED data in the near-infrared range (Section 2.2).

[2] http://www.aips.nrao.edu/index.shtml
[3] https://casa.nrao.edu/index.shtml
[4] http://galex.stsci.edu/GR6/

There are usually no high-resolution images of typical spherical AGB stars, therefore we selected such control objects from the SiO maser sources. Our control AGB stars all exhibit a sharp single-peaked SiO maser feature (Nakashima & Deguchi 2003). This is good evidence showing that the corresponding envelopes are spherical, because this type of maser spectral profile is produced when the masers are tangentially amplified in the spherical envelope. For the control post-AGB stars, IRAS 07134+1005 is suggested to have a geometrically thick expanding torus (Nakashima et al. 2009); IRAS 22272+5435 is so far best interpreted as a system consisting of a spherical wind, torus and a jet interacting with ambient materials (Nakashima et al. 2012). The aspherical structures of both objects have been revealed via interferometric observations of the CO line. The other four post-AGB stars were selected from the infrared image catalogue presented in Lagadec et al. (2011). Both IRAS 17534+2603 and IRAS 20547+0247 are unresolved objects, which could mean that either they are spherical or they are too far away. OH 231.8+4.2 and IRAS 17441−2441 show aspherical features in the images. Table 1 (Column 4) lists the morphologies of all the control objects.

The DUSTY models used and the fitting procedures for the control objects were the same as those for the WFs. The only exceptions were IRAS 07134+1005 and IRAS 22272+5435. Owing to their carbon-rich nature, a grain type of 90 per cent amorphous carbon (Hanner 1988) and 10 per cent SiC (Pegourie 1988) was used instead of silicates for their DUSTY models. We have confirmed that, as long as the optical depth is not too large (e.g. $\tau_{2.2} < 1$), the emission features of carbonaceous compounds will not be prominent and hence the SED profile shape of the carbon- and oxygen-rich envelopes is very similar.

3 RESULTS AND INTERPRETATION

3.1 Types of profile

There are three types of SED profile.

(1) The envelope is spherical and the SED can be fitted by a DUSTY model with either a single-peaked (denoted by 'S' in Tables 1 and 3) or double-peaked ('D') profile. A single-peaked profile means the envelope is not detached, e.g. in cases of usual AGB stars. A double-peaked profile means the envelope is detached, which is a characteristic of post-AGB stars. In such cases, the near-infrared peak is mainly contributed by the reddened photosphere of the central star and the far-infrared peak is attributed to the cold dust in the detached envelope (Kwok 1993).

(2) Some data points in the mid- to far-infrared range can be fitted by DUSTY, but the near-infrared data cannot. Each of these SEDs has either a near-infrared flux deficit ('ND') or excess ('NE') compared with the corresponding closest model curves. According to Lagadec et al. (2011), the near-infrared excess could be caused by the emission from hot dust close to the star and the envelope of such a star is likely bipolar; the near-infrared deficit could be the result of a thick torus that absorbs radiation. In both cases the envelopes are aspherical and hence no good fits can be obtained for the entire SED.

(3) This type of SED is similar to (2). The major difference is that in this case the near-infrared data points are not too reliable, due to heavy interstellar extinction, hence it is difficult to judge whether they have infrared excess or deficit. These envelopes are also likely aspherical.

Table 3. DUSTY parameters of each object that has a good model fit for the SED (See Table 1).

Object	Profile[a]	$T_{\rm eff}$ (K)	$T_{\rm d}$ (K)	$\tau_{2.2}$
	Water fountains			
IRAS 18113−2503	D?	4400	100	0.700
OH 12.8−0.9	S	2200	700	3.000
IRAS 18455+0448	S	4400	600	2.000
IRAS 19356+0754	D	2000	200	2.000
	Control AGB stars			
IRAS 14247+0454	S	2400	400	0.045
IRAS 18556+0811	S	2400	700	0.300
IRAS 19149+1638	S	2000	700	0.450
IRAS 19312+1130	S	2000	800	0.300
IRAS 19395+1827	S	2200	500	0.100
IRAS 19495+0835	S	2000	700	0.450
	Control post-AGB stars			
IRAS 17534+2603	S?	3400	1600	1.000
IRAS 20547+0247	S?	3600	900	4.000
IRAS 22272+5435[b]	D	8200	200	0.010

Notes. [a]SED profiles are classified into single-peaked 'S' or double-peaked 'D'. An extra '?' means that the SED is marginally fitted by the model.
[b]Carbon-rich objects. The dust component parameters used in the DUSTY model are different from those of other oxygen-rich objects. See text for details.

3.2 Control objects

All of our control AGB stars exhibit a single-peaked SED profile and good fits could be obtained from DUSTY models (Fig. 1). Table 3 gives the corresponding DUSTY parameters. The maximum flux is found in the near-infrared region, at about 2 μm. This is common for AGB stars according to previous studies (e.g. Groenewegen 1995). The temperatures for the best-fitting models are as follows: 2000 K $\leq T_{\rm eff} \leq$ 2400 K; 400 K $\leq T_{\rm d} \leq$ 800 K. The optical depths ($\tau_{2.2}$) are mostly in range 0.1–0.5. Usually the larger the optical depth, the more prominent the 9-μm silicate emission feature.

For the control post-AGB stars, there are no good fits for the SEDs of IRAS 07134+1005, OH 231.8+4.2 and IRAS 17441−2411 (Fig. 2). This is not unexpected, because their envelopes are aspherical, as shown in the infrared image catalogue from Lagadec et al. (2011). IRAS 17534+2603 and IRAS 20547+0247 are two unresolved objects from the same catalogue, which means they could have spherical envelopes or else they are too far away. Both SEDs could be marginally fitted by DUSTY with single-peaked models. It is possible that their envelopes have just started to depart from spherical symmetry and hence the aspherical features are not revealed in images. IRAS 22272+5435 is the only post-AGB star with a good fit here. The effective temperature obtained ($T_{\rm eff} = 8200$ K) is higher than that of AGB stars, but the dust temperature ($T_{\rm d} = 200$ K) is lower. This is expected for a post-AGB star where the central star is becoming hotter, while the detached dust envelope is expanding and becoming cooler. The temperatures obtained are similar to some post-AGB stars modelled by DUSTY as presented in Surendiranath, Parthasarathy & Varghese (2002). The best-fitting optical depth is $\tau_{2.2} = 0.01$. Note that our $T_{\rm eff}$ is higher than the result from Szczerba et al. (1997), who found $T_{\rm eff} = 5300$ K. The discrepancy is due mainly to the different extinction values used, which affects the fluxes at short wavelengths that constrain the stellar temperature. Szczerba et al. (1997) adopted $A(V) = 1.0$ and 2.0, while we estimated $A(V) = 5.537$. Since this object is known to have aspherical envelope features revealed by CO (see Section 2.4), it may seem

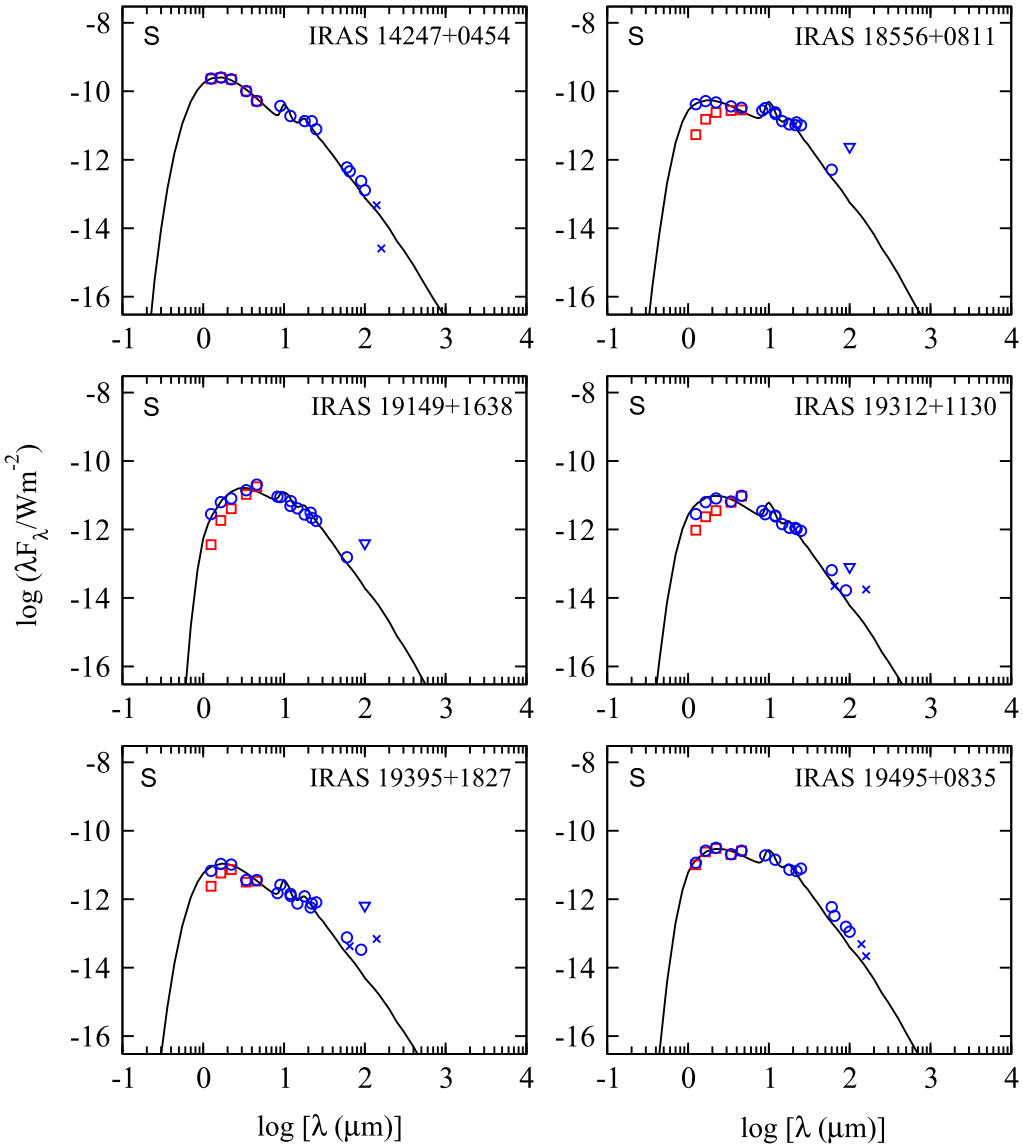

Figure 1. Spectral energy distributions of some standard AGB stars with spherical envelopes. The squares represent original data points without correction for interstellar extinction (only for data with wavelengths shorter than 8 μm), while the circles represent data points we actually used for analysis. The lower and upper limits of the fluxes are indicated by upward and downward triangles, respectively. Flux values with a low-quality flag are indicated by crosses. The curves represent the best-fitting models with the DUSTY code (see text for details). For each case where a good fit is available, 'S' denotes a single-peaked profile, 'D' denotes a double-peaked profile and an extra '?' means the SED is marginally fitted by the model. For each case without a good fit, 'NE' denotes a profile with near-infrared excess and 'ND' denotes near-infrared deficit.

odd that a good fit is available, in particular when comparing it with the similar case IRAS 07134+1005. This can actually be explained by the fact that, via CO emission, the existence of a spherical shell is predicted and the torus found in this object is several times smaller than that in IRAS 07134+1005 (Nakashima et al. 2012). Hence it is likely that the molecular distribution in the outer envelope of IRAS 22272+5435 still remains mostly undisturbed, but this is not the case for IRAS 07134+1005.

As a result, it can be seen that that our method is in general able to reproduce known results quite accurately: good fits for spherical envelopes, but not for aspherical envelopes. Nonetheless, we notice that the SEDs of envelopes with aspherical features could sometimes still be reproduced by one-dimensional models, depending on how large and significant the aspherical features are. Therefore the logic is that, if a good fit is obtained, then it is very likely that the envelope is spherical, though it is not guaranteed; however, if no good fit could be obtained then it is quite certain that the envelope is really aspherical, subject to some restrictions discussed in Section 2.3.

3.3 Water fountains

3.3.1 Overview

The 17 WFs or WF candidates show a variety of SED profiles (Table 1). Good DUSTY fits are obtained for four WF SEDs and they are classified into two categories: single-peaked or double-peaked profiles. Two of the SEDs could be fitted by single-peaked model curves (OH 12.8−0.9 and IRAS 18455+0448). These two objects are found to be relatively young WF members, i.e. AGB or early

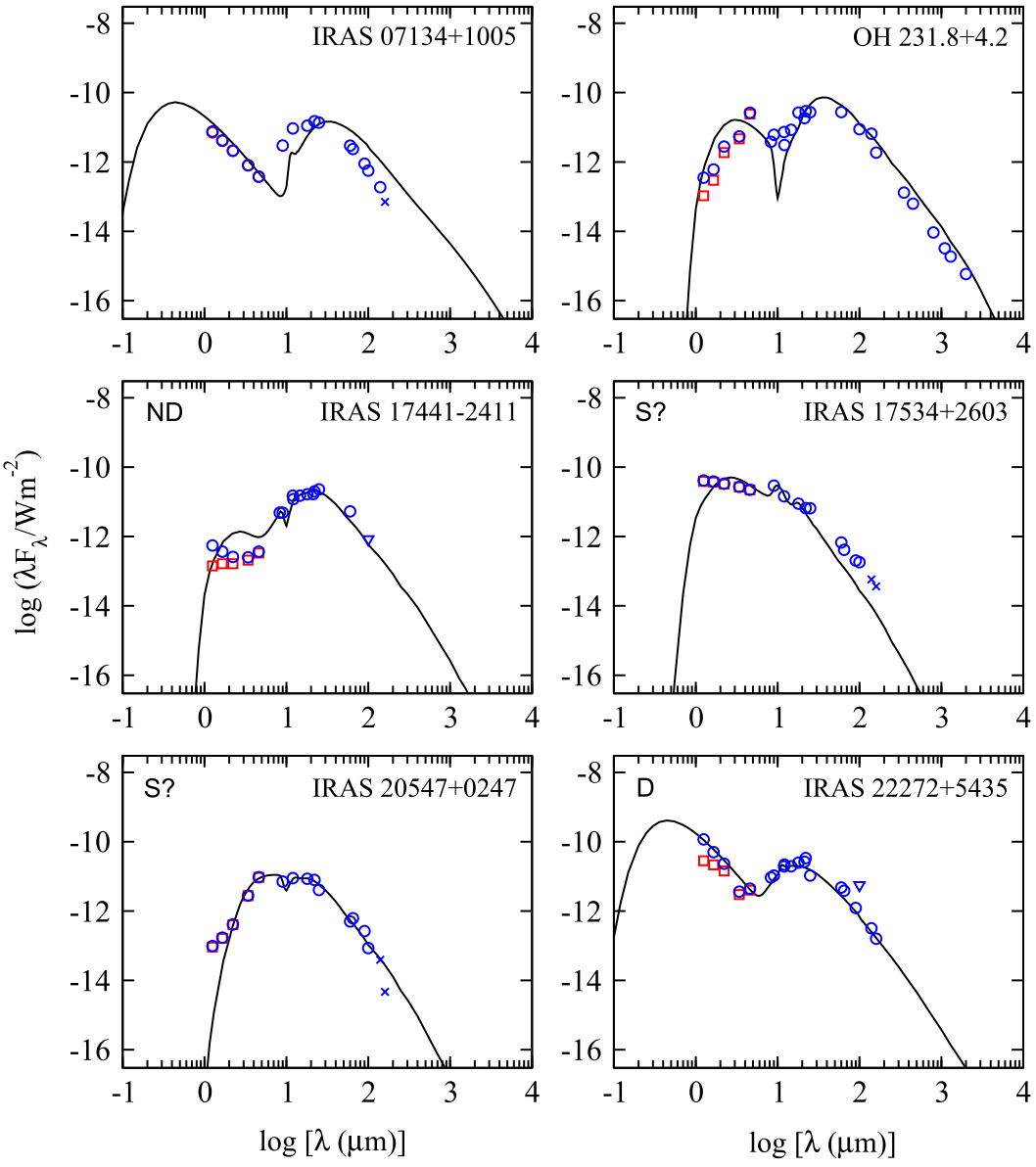

Figure 2. Spectral energy distributions of some post-AGB stars with aspherical structures, for e.g. tori or jets. The notations used in this figure are the same as in Fig. 1.

post-AGB stars. Another two WFs could arguably be fitted by double-peaked curves (IRAS 18113−2503 and IRAS 19356+0754). These are likely to be post-AGB stars. Some of the data points in these cases seem to deviate from the model curves, but we notice that the curves still reproduce the SED line shapes reasonably, thus we treat them as cases that are fitted.

On the other hand, as mentioned in Section 1, a number of WFs are known to have bipolar structures from infrared images. Those are the cases that could not be fitted by DUSTY, as expected. For these 13 SEDs without good fits, more than a few of them share a similarity: there is a peak in the mid- to far-infrared range that could be fitted by DUSTY, but the near-infrared data cannot be fitted. Each of these particular SEDs has either a near-infrared deficit or an excess in comparison with the corresponding closest model curves. All these cases without good fits are likely to be post-AGB stars with aspherical envelope features. Note again that there is strong near-infrared extinction towards some objects and for those cases the fits are not reliable either.

Some objects have different flux values from similar wavelength bands. A major reason is the difference in measured aperture size adopted from different instruments accounting for those bands. Another possible reason is that those objects may have a certain degree of variability. Nonetheless, we found that the small deviations do not affect our fitting results when there are enough data points for constructing the SEDs.

Column 4 of Table 1 gives the morphologies of the objects according to infrared images, if any; column 5 gives a summary on whether the objects could be fitted and which categories the objects have fallen into. Table 3 lists the best-fitting DUSTY parameters ($T_{\rm eff}$, $T_{\rm d}$ and $\tau_{2.2}$) for the objects with good fits. The SEDs and DUSTY model curves with the smallest sum of least-squares values are shown in Fig. 3.

3.3.2 Single-peaked SED profiles

The SEDs of OH 12.8−0.9 and IRAS 18455+0448 could be fitted by single-peaked DUSTY models, which look similar to AGB stars, but they are still distinguishable because the peaks of these WF SEDs are shifted to the mid-infrared region. This shift is primarily due to the large amount of cold dust in the thicker envelopes, which also accounts for their large $J - K$ colour. The fact that these two WFs could be fitted by the one-dimensional code means that they probably have envelopes that are close to spherical. Recall that WFs are objects associated with bipolar jets that can be traced by H_2O maser emission. Intuitively, they must be aspherical objects. However, the physical length of one side of the maser jet is typically of order 10^2–10^3 au, as mentioned earlier, but the envelope of a standard AGB star could have a radius of about 10^5 au (Habing 1996). Hence, if no other form of large aspherical feature is present (see Section 4), it is possible that, even though a WF jet has already formed, the outer part of the envelope, which can be observed in the mid- to far-infrared, still remains spherical.

The relatively low $T_{\rm eff}$ (2200 K) of OH 12.8−0.9 is similar to those of the control AGB stars, indicating this object is likely still in the AGB phase. The H_2O maser velocity coverage of this object is relatively small within the WF class, ∼48 km s^{-1}, and the three-dimensional jet velocity is estimated to be 58 km s^{-1} (Boboltz & Marvel 2007), which is the slowest jet velocity found in WFs. Jet acceleration was observed to be happening for this object and therefore we suggest it is a relatively young WF (under the assumption that jets may accelerate as they develop).

IRAS 18455+0448 was reported as a low-velocity WF candidate with velocity coverage <40 km s^{-1} (Yung et al. 2013). Its 1612-MHz OH maser profile was analysed by Lewis, Oppenheimer & Daubar (2001), who found that the double-peaked feature had been fading over a period of 10 years; this object was argued to be a very young post-AGB star. Its H_2O maser emission was analysed further by Vlemmings et al. (2014) via interferometric observations, which confirmed its WF status. IRAS 18455+0448 has a higher $T_{\rm eff}$ (4400 K) than the AGB stars, implying that it could be slightly more evolved, which again agrees with the discussions in Lewis et al.

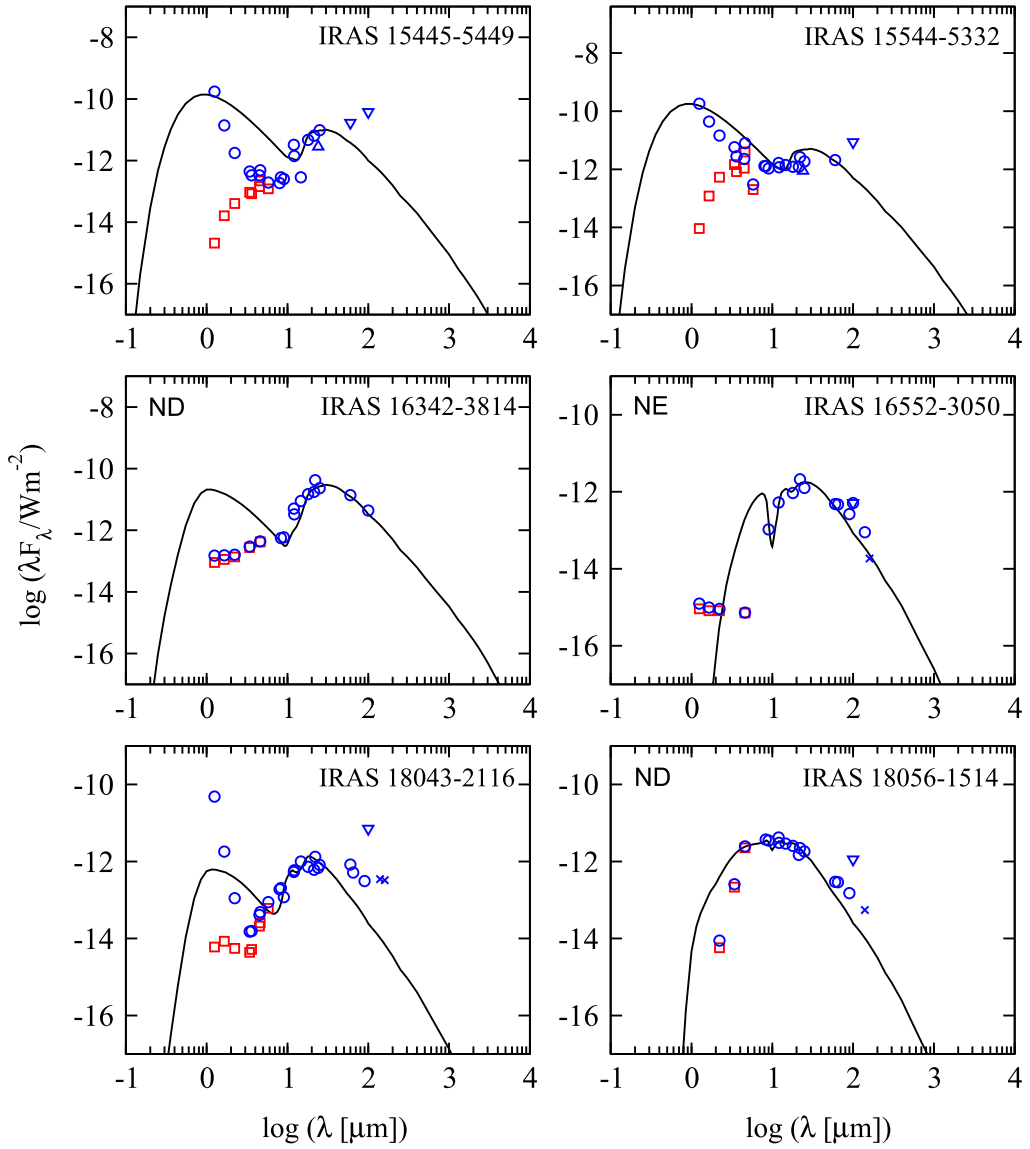

Figure 3. Spectral energy distributions of the water fountains. The notations used in this figure are the same as in Fig. 1.

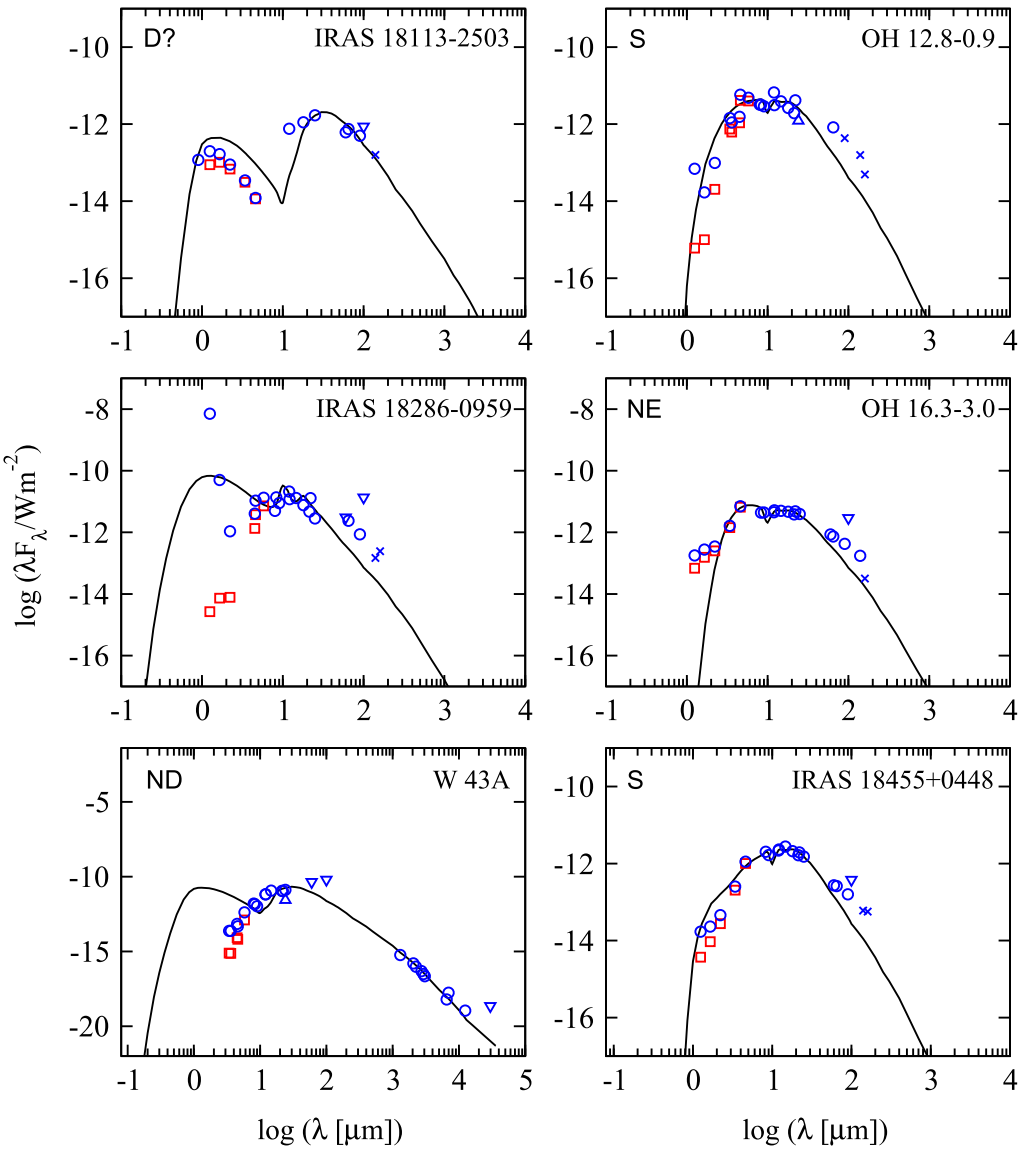

Figure 3 – *continued*

(2001) and Yung et al. (2013). Similarly to OH 12.8−0.9, the H_2O maser kinematics and the SED profile of IRAS 18455+0448 give the same prediction that this object could be a younger member of the WF class.

3.3.3 *Doubled-peaked SED profiles*

There are two WFs with double-peaked SEDs that could arguably be fitted by DUSTY. The double-peaked profile is a characteristic of post-AGB stars, as mentioned earlier. Both WFs have larger optical depths than the control AGB stars, which is another hint that they could be more evolved objects with thicker envelopes.

IRAS 18113−2503 has the largest velocity coverage (∼500 km s^{-1}) of H_2O maser emission amongst all WFs (Gómez et al. 2011). The three-dimensional jet velocity is not known, but from this large spectral velocity coverage it is possible that this object has the fastest WF jet. No OH maser observation has been performed towards this object, so the kinematical condition of the outer envelope is not known. We considered the SED of this object as marginally fitted, because the model curve is able to reproduce the general line shape and the double-peaked feature with a brighter cold peak. Nonetheless, the deviation from some data points indicates that the envelope is perhaps not totally spherical. Gómez et al. (2011) proposed that this object is a post-AGB star, based on the infrared characteristics.

IRAS 19356+0754 is a WF candidate that has a rather irregular OH maser profile (Yung et al. 2014). Its *IRAS* colours suggest that it should be a (Mira) variable star at the end of the mass-loss phase, which has a very thick oxygen-rich envelope (Region IV in van der Veen & Habing 1988). These properties show that the object should be a late/post-AGB star. However, the best-fitting DUSTY model for the SED gives $T_{\rm eff} \sim 2000$ K, which is unexpectedly low for such an evolved object. It is possible that this star is undergoing a third dredge-up, which would cool down its effective temperature significantly due to the sudden increase of atmospheric opacity (e.g. Herwig 2005). More evidence is needed to confirm the true status of this object.

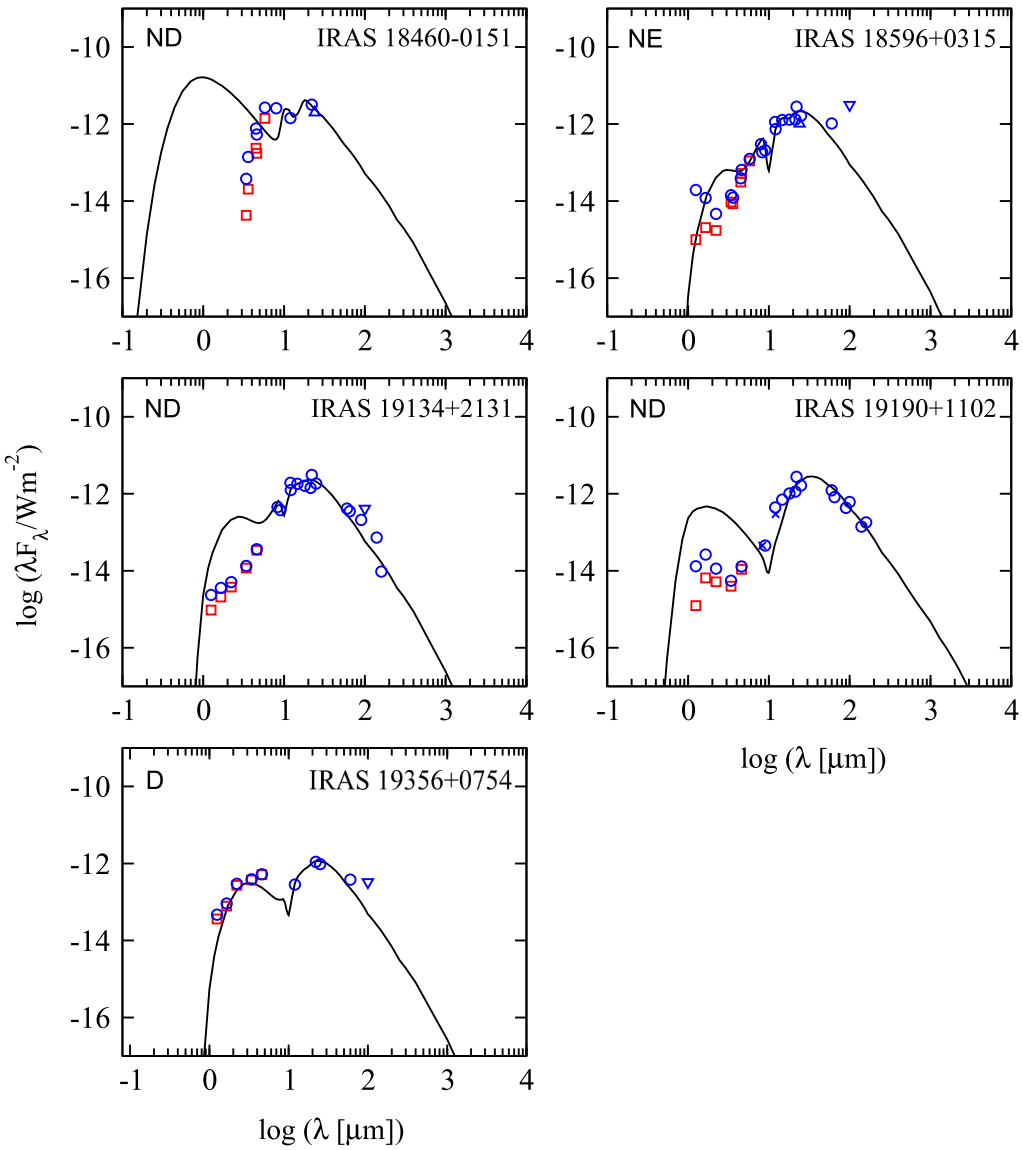

Figure 3 – *continued*

3.3.4 SED profiles without good fits

No good fits from DUSTY models could be obtained for 13 WFs or WF candidates. Some of them are known to have well-developed bipolar structures in infrared wavelengths, such as IRAS 15445−5449 (Lagadec et al. 2011; Pérez-Sánchez, Vlemmings & Chapman 2011; Pérez-Sánchez et al. 2013) and IRAS 16342−3814 (Sahai et al. 1999). The deviation from the DUSTY best-fitting model is mainly due to the non-spherical structure of the envelopes. It is found that more than half of these unfit SEDs have a near-infrared deficit compared with the model curves. The objects showing this feature are IRAS 15445−5449, IRAS 16342−3814, IRAS 18460−0151, IRAS 19314+2131 and IRAS 19190+1102 (see Fig. 3). Using IRAS 16342−3814 as a case study, Murakawa & Izumiura (2012) suggested that this type of SED could be reproduced by a model consisting of a spherical AGB envelope, an optically thick torus and a bipolar jet. This is a typical post-AGB star structure and this means that most of the unfitted WFs could already have evolved into the post-AGB phase, except for the known example of W43A (Imai et al. 2002) and a possibly new example, IRAS 18056−1514 (see below), which seem to be AGB stars with aspherical envelopes.

The three objects IRAS 16552−3050, OH 16.3−3.0 and IRAS 18596+0315 are a bit different from the above. The near-infrared fluxes of the former two objects reveal plateau features, which are brighter than the model curves (see Fig. 3). This near-infrared excess could be a result of hot dust or the existence of circumstellar discs (e.g. Gezer et al. 2015), or from possible hot companions. IRAS 18596+0315 shows not a plateau in the near-infrared range, but an increasing slope towards shorter wavelengths (Fig. 3). It is unsure whether this feature is reliable due to strong extinction. Its WF status was first suggested by (Engels 2002). An interferometric observation of the OH maser reveals a slightly bipolar structure (Amiri, Vlemmings & van Langevelde 2011) and again this is a signature of the envelope departing from spherical symmetry.

It is difficult to judge whether IRAS 15544−5332 has a good SED fit or not. The reason is that most of the reliable data points are clustered in a relatively small mid-infrared range and the near-infrared data points are not fully reliable, due to strong extinction

(Fig. 3). Therefore the result is inconclusive, but we conservatively put it as an unfitted case. This is a WF candidate with only one H_2O maser emission peak found outside the velocity coverage of its OH maser, which has a slightly irregular double-peaked profile (Deacon, Chapman & Green 2007). An irregular OH maser profile indicates that the outer envelope has been disturbed (e.g. by jets) so that it is no longer spherical (Zijlstra et al. 2001). In this case, the envelope might have just started to depart from spherical symmetry, thus the double-peaked OH maser profile has not been totally broken down. The SED profile tells a similar story, as the marginally fitted model curve could imply that the possibly detached/detaching AGB envelope is about to become aspherical.

IRAS 18056−1514 is an odd case here. No good fit is obtained, but the closest model curve is single-peaked and looks like that for OH 12.8−0.9. There is no further study regarding IRAS 18056−1514 and in fact its WF status remains very doubtful. This is because its only H_2O maser emission peak found outside the OH velocity range (Yung et al. 2013) was not present in a later observation (Yung et al. 2014). This object is likely to be a late AGB star according to the infrared colours and this agrees with its single-peaked SED profile.

4 DISCUSSION

We have shown that good DUSTY fits could be obtained for some WF SEDs, implying spherical envelopes, but others are likely associated with aspherical envelopes. The results suggest that even though all WFs possess maser jets with apparently similar dynamical ages, the objects could be coming from different stages of morphological metamorphosis. Since this change in morphology is known to be closely related to the evolutionary status, our results also imply the fact that WFs could have different evolutionary statuses. This fact agrees with other evidence such as the colours of the objects. Note that it might be difficult to determine whether the SED fits are good for several WFs, but the remaining unambiguous cases are sufficient to support the above ideas. There are several details requiring deeper exploration regarding the role of WFs. In this section, we will discuss the problem of the definition of dynamical ages and also the possible relationship between WF jets and other types of outflow.

4.1 Dynamical age

The main reason that WFs are regarded as objects starting to deviate from spherical symmetry is the short dynamical age of their jets. This contradicts the results of the present study. If WF jets really indicate the earliest moment of such envelope morphological change, we expect that the majority of WFs would still have rather spherical envelopes. This is because WF jets are small in scale (see Section 1) and hence probably could not disturb the outer infrared envelope so much within less than 100 years. We suggest that this contradiction arisen from the method used to define and estimate the dynamical ages of WF jets.

The usual method is to perform multi-epoch very long baseline interferometry observations to measure the proper motions on the sky plane of individual H_2O maser features (see e.g. Imai, Sahai & Morris 2007; Yung et al. 2011). Then the jet dynamical age is estimated from the observed spatial extent of the jet (traced by the maser feature distribution) and the jet velocity on the sky plane. However, whether this is the real age of the jet is not guaranteed. This method of estimation assumes that maser features are able to trace the tip of the jet. In fact, the maser features could be tracing only the innermost part of the entire jet. It is possible that the tip of the jet has arrived at the more outer region of the envelope, but cannot be seen in maser observations. This could happen because H_2O molecules are more abundant in the inner region (within hundreds of au from the central star) of the envelope and hence easier to observe via maser emission.

The dynamical age calculated with the above method therefore does not have a real physical meaning and hence not all WFs are really the 'transitional objects' that we have been looking for. Furthermore, it is actually questionable whether the larger jets or bipolar structures observed in infrared images (e.g. Lagadec et al. 2011) must be developed from smaller jets such as WF jets. Nonetheless, this class of object is still very valuable, because the maser emission allows us to look deep into the root of bipolar jets, which could provide essential physical constraints for understanding the jet formation mechanism.

4.2 Torus

According to our results, WFs could be objects from different morphological metamorphosis stages. In this subsection, we try to speculate how this could be possible. We should note that jets are not the only type of aspherical outflow that affects an envelope's morphology. Observations have shown that an AGB/post-AGB star with bipolar jet is very likely to be associated with a torus. The torus is suggested to appear quite 'suddenly' within a short time and the jet is formed almost simultaneously or shortly after the formation of the torus (e.g. by a few hundred years, Huggins 2007). Here, the 'jet' does not refer only to the specific small-scale WF jets, but also stellar jets in general, which could be much larger in scale. Such a torus–jet configuration is currently best described by the existence of a binary component around the primary AGB/post-AGB star (see Huggins 2007, and the references therein).

If this is the case, then WFs are expected to be associated with tori as well. In fact, the existence of tori has been proposed for W43A (Imai et al. 2005) according to the distribution of the SiO maser and for IRAS 16342−3814 (Verhoelst et al. 2009) because of the 'dark waist' observed in mid-infrared images. IRAS 18286−0959 has a few outlier H_2O maser features observed in the equatorial region (Imai et al. 2013a), which might be related to a torus as well. There is no such evidence found for other WFs so far; however, we suggested that some of the unfitted SEDs could result from a well-developed torus feature. As discussed in Section 3.2, both of our control post-AGB stars IRAS 07134+1005 and IRAS 22272+5435 are known to have a torus, but only the former has an SED unfitted by DUSTY. This is very likely related to the size of their corresponding tori. In addition, the near-infrared plateau features observed in some WFs mentioned in Section 3.3.4 could also be related to disc-like features (Gezer et al. 2015) and/or hot companions.

Fig. 4 shows a possible scenario putting the torus, WF maser jet and larger jet together. Note that, even though it has been generally believed that jets grow from the smallest sizes (see Section 1), there is in fact no concrete evidence showing that this is the only possible way for jets to develop. The only evidence is perhaps the existence of WFs with spherical envelopes (Section 3.3.2), which show that no larger jet structure is present yet, but this evidence alone is not strong enough to be conclusive. Therefore, step (b) shown in Fig. 4 may not be necessary. If this step does exist, then some of the WFs may really be objects possessing young jets; if this step does not exist, then there is no way to tell from the WF jets the real age of the entire jet. In either case, the WF jets trace the innermost part of the entire jet in this scenario.

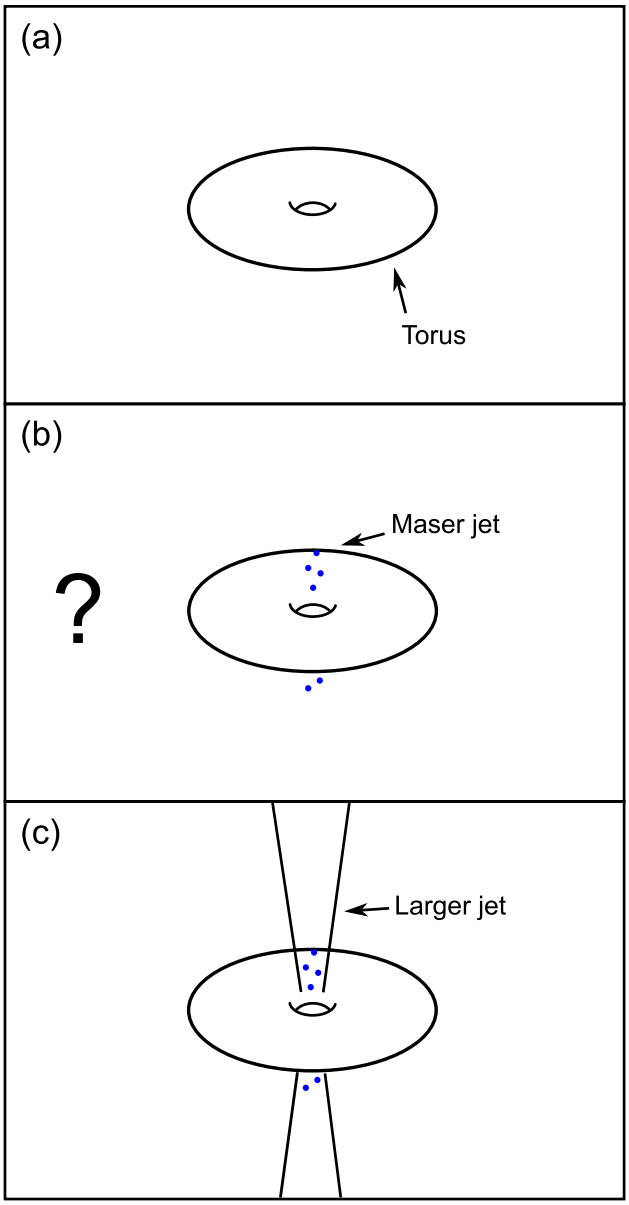

Figure 4. Schematic view of a possible evolutionary sequence starting with (a) the formation of a torus, followed by (b) a water-fountain maser jet and then (c) a larger jet. Note that it is unclear whether the small-scale maser jet must exist earlier than the larger jet or whether they could coexist from the beginning. Step (b) might be omitted.

4.3 Extreme outflow

Another type of outflow comprises the molecular jets that can usually be traced by thermal line emission from CO molecules, for which Sahai & Patel (2015) have coined the term 'extreme outflow'. These jets could have velocities >100 km s^{-1}, similar to WF jets, but with larger physical sizes (see Section 1). The relationship between WF jets and extreme outflows is unclear, because so far the latter have not been detected towards WFs; this is probably due to sensitivity constraints and foreground/background contamination (Rizzo et al. 2013). However, a comparison of the jet orientations of WF jets, extreme outflows and large infrared bipolar structures may give us some hints.

It is found that the orientations of extreme outflows align with the possibly bipolar envelopes of the corresponding objects as shown in the optical/infrared images (Olofsson et al. 2015; Sahai & Patel 2015). The estimated momentum of the outflow was too large to be supported by radiation pressure from the central star and hence a mechanism driven by a binary system is more plausible (Sahai & Patel 2015), similar to that discussed in Section 4.2. Therefore it is likely that extreme outflows have a direct connection to the shaping of such aspherical envelopes. Similarly, for the WFs IRAS 15445−5449 (Pérez-Sánchez et al. 2013), IRAS 16342−3814 (Sahai et al. 1999) and W43A (Imai et al. 2002), the spatial extent of their envelopes in infrared images (even in the optical for the case of IRAS 16342−3814) aligns very well with their corresponding WF maser jets. Other WFs are either unobserved or unresolved in infrared imaging.

From these comparisons, it is not surprising that both extreme outflows and WF jets have a connection to large bipolar structures. An intuitive guess is that these two types of jet could even be aligned. However, we arrive at the same problem, i.e. whether the smaller WF jets are younger versions of the larger extreme outflows. If this is true, then an extreme outflow might represent a chronological stage somewhere between Fig. 4(b) and (c), but we do not have sufficient information to examine this.

5 CONCLUSIONS

We suggest that the various morphologies of PNe are shaped by high-velocity bipolar jets from (late) AGB and post-AGB stars. It has been widely believed that such jets develop from tiny young jets such as those from WFs. Hence WFs are regarded as objects representing the onset of the morphological change of envelopes. However, there is no concrete evidence supporting this hypothesis. We performed a collective study of SED profiles by fitting one-dimensional dust radiative transfer models generated by the DUSTY code. Our objects included confirmed WFs, as well as a few WF candidates (17 objects in total). We have also studied some known AGB and post-AGB stars as control objects. Our findings are summarized as follows.

(i) The SED profiles of two WFs could be fitted by single-peaked DUSTY models which are all peaked in the mid-infrared range. Another two could arguably be fitted by double-peaked models resembling those for the post-AGB stars. No good fits could be obtained for the remaining 13 WFs; more than half of these objects exhibit double-peaked line shapes with the near-infrared peak significantly weaker than the far-infrared peak. The results confirm that WFs could possess different envelope morphologies and hence it is unlikely that they must be objects just starting to deviate from spherical symmetry, as previously believed.

(ii) The short dynamical age of WFs has no real physical meaning and it cannot be used as evidence to claim that WF jets must be young. WF jets could be the innermost part of well-developed larger jets.

(iii) The role of WF jets is discussed, together with other common aspherical envelope components such as tori and the molecular jets revealed by CO thermal line emission ('extreme outflows'). According to existing observations and theories, it is likely that tori will be formed ahead of jets, but whether there is any chronological relationship between WF jets and extreme outflows is unclear. Both types of jet are shown to be correlated with the large-scale bipolar structure revealed in infrared observations for some objects.

The present work is also the pioneer collective study of WF envelopes by simple but effective one-dimensional radiative transfer

models. We suggest that this approach will be useful for future statistical studies of a larger number of stellar maser sources.

ACKNOWLEDGEMENTS

This work is supported by Act 211 Government of the Russian Federation, agreement No. 02.A03.21.0006a. JN is supported by grants from the Research Grants Council of Hong Kong (project code: HKU 704411P) and the Small Project Funding of the University of Hong Kong (project code: 201007176004). CHH is supported by the Small Project Funding of the University of Hong Kong (project No. 201007176028) and the Science and Technology Development Fund of Macau (project code: 039/2013/A2 and 017/2014/A1). The Laboratory for Space Research was established by a special grant from the University Development Fund of The University of Hong Kong. This work is also in part supported by grants from the HKRGC (HKU 7027/11P and HKU 7062/13P). This publication makes use of data products from the following: Two-Micron All Sky Survey, which is a joint project of the University of Massachusetts and the Infrared Processing and Analysis Center/California Institute of Technology, funded by the National Aeronautics and Space Administration and the National Science Foundation; *Wide-field Infrared Survey Explorer*, which is a joint project of the University of California, Los Angeles and the Jet Propulsion Laboratory/California Institute of Technology, funded by the National Aeronautics and Space Administration; *Midcourse Space Experiment*, processing of the data was funded by the Ballistic Missile Defense Organization with additional support from NASA Office of Space Science; NASA/IPAC Infrared Science Archive, which is operated by the Jet Propulsion Laboratory, California Institute of Technology, under contract with the National Aeronautics and Space Administration; *Infrared Astronomical Satellite* (*IRAS*), a joint project of the US, UK and the Netherlands; *AKARI*, a JAXA project with the participation of ESA; *Spitzer Space Telescope*, which is operated by the Jet Propulsion Laboratory, California Institute of Technology under a contract with NASA. The National Radio Astronomy Observatory is a facility of the National Science Foundation operated under cooperative agreement by Associated Universities, Inc. The Nobeyama Millimeter Array was operated by Nobeyama Radio Observatory, a branch of National Astronomical Observatory of Japan, National Institutes of Natural Sciences.

REFERENCES

Amiri N., Vlemmings W., van Langevelde H. J., 2011, A&A, 532, A149
Boboltz D. A., Marvel K. B., 2007, ApJ, 665, 680
Day F. M., Pihlstrom Y. M., Claussen M. J., Sahai R., 2010, ApJ, 713, 986
Deacon R. M., Chapman J. M., Green A. J., 2007, ApJ, 658, 1096
Desmurs J.-F., 2012, in Booth R. S., Humphries E. M. L., Vlemmings W. H. T., eds, IAU Symp. 287, Cosmic Masers - from OH to H_0. Cambridge University Press, Cambridge, p. 217
Egan M. P. et al., 2003, The Midcourse Space Experiment Point Source Catalog Version 2. 3 Explanatory Guide. Storming Media, Washington, DC
Engels D., 2002, A&A, 388, 252
Fazio G. G. et al., 2004, ApJS, 154, 10
Gezer I., Van Winckel H., Bozkurt Z., De Smedt K., Kamath D., Hillen M., Manick R., 2015, MNRAS, 453, 133
Gómez J. F., Rizzo J. R., Suárez O., Miranda L. F., Guerrero M. A., Ramos-Larios G., 2011, ApJ, 739, L14
Gómez J. F., Rizzo J. R., Suárez O., Palau A., Miranda L. F., Guerrero M. A., Ramos-Larios G., Torrelles J. M., 2015a, A&A, 578, A119
Gómez J. F. et al., 2015b, ApJ, 799, 186
Groenewegen M. A. T., 1995, A&A, 293, 463
Habing H. J., 1996, A&AR, 7, 97
Hanner M. S., 1988, NASA Conf. Pub., 3004, 22
Herman J., Habing H. J., 1985, A&AS, 59, 523
Herwig F., 2005, ARA&A, 43, 435
Hirano N. et al., 2004, ApJ, 616, L43
Howarth I. D., 1983, MNRAS, 203, 301
Hsia C.-H., Zhang Y., 2014, A&A, 563, A63
Huggins P. J., 2007, ApJ, 663, 342
Imai H., 2007, in Baan W., Chapman J., eds, IAU Symp. 242, Astrophysical Masers and Their Environments. Cambridge University Press, Cambridge, p. 279
Imai H., Obara K., Diamond P. J., Omodaka T., Sasao T., 2002, Nature, 417, 829
Imai H., Nakashima J., Diamond P. J., Miyazaki A., Deguchi S., 2005, ApJ, 622, L125
Imai H., Sahai R., Morris M., 2007, ApJ, 669, 424
Imai H., Nakashima J., Yung B. H. K., Deguchi S., Kwok S., Diamond P. J., 2013a, ApJ, 771, 47
Imai H., Deguchi S., Nakashima J., Kwok S., Diamond P. J., 2013b, ApJ, 773, 182
Ivezić Ž., Nenkova M., Elitzur M., 1999, User Manual for dusty, University of Kentucky Internal Report. Available at: http://www.pa.uky.edu/∼moshe/dusty/manual.html
Kataza H. et al., 2010, AKARI-FIS Bright Source Catalogue Release note Version 1.0. ISAS, Sagamihara
Kwok S., 1993, ARA&A, 31, 63
Kwok S., 2010, PASA, 27, 174
Lagadec E. et al., 2011, MNRAS, 417, 32
Lewis B. M., Oppenheimer B. D., Daubar I. J., 2001, ApJ, 548, 77
Mathis J. S., Rumpl W., Nordsieck K. H., 1977, ApJ, 217, 425
Monnier J. D., Tuthill P. G., Danchi W. C., 2000, ApJ, 545, 957
Murakawa K., Izumiura H., 2012, A&A, 544, A58
Nakashima J., 2005, ApJ, 620, 943
Nakashima J., Deguchi S., 2003, PASJ, 55, 229
Nakashima J., Koning N., Kwok S., Zhang Y., 2009, ApJ, 692, 402
Nakashima J., Koning N., Volgenau N. H., Kwok S., Yung B. H. K., Zhang Y., 2012, ApJ, 759, 61
Neugebauer G. et al., 1984, ApJ, 278, L1
Olofsson H., Vlemmings W. H. T., Maercker M., Humphreys E. M. L., Lindqvist M., Nyman L., Ramstedt S., 2015, A&A, 576, L15
Ossenkopf V., Henning T., Mathis J. S., 1992, A&A, 261, 567
Pegourie B., 1988, A&A, 194, 335
Pérez-Sánchez A. F., Vlemmings W. H. T., Chapman J. M., 2011, MNRAS, 418, 1402
Pérez-Sánchez A. F., Vlemmings W. H. T., Tafoya D., Chapman J. M., 2013, MNRAS, 436, L79
Ramos-Larios G., Guerrero M. A., Suárez O., Miranda L. F., Gómez J. F., 2012, A&A, 545, A20
Rieke G. H. et al., 2004, ApJS, 154, 25
Rizzo J. R., Gómez J. F., Miranda L. F., Osorio M., Suárez O., Durán-Rojas M. C., 2013, A&A, 560, A82
Sahai R., Patel N. A., 2015, ApJ, 810, L8
Sahai R., Trauger J. T., 1998, AJ, 116, 1357
Sahai R., te Lintel Hekkert P., Morris M., Zijlstra A., Likkel L., 1999, ApJ, 514, L115
Sahai R., Morris M. S. C. C., Claussen M., 2007, AJ, 134, 2200
Schlafly E. F., Finkbeiner D. P., 2011, ApJ, 737, 103
Schlegel D. J., Finkbeiner D. P., Davis M., 1998, ApJ, 500, 525
Siódmiak N., Meixner M., Ueta T., Sugerman B. E. K., Van de Steene G. C., Szczerba R., 2008, ApJ, 677, 382
Skrutskie M. F. et al., 2006, AJ, 131, 1163
Suárez O., Gómez J. F., Miranda L. F., 2008, ApJ, 689, 430
Suárez O., Gómez J. F., Miranda L. F., Torrelles J. M., Gómez Y., Anglada G., Morata O., 2009, A&A, 505, 217
Surendiranath R., Parthasarathy M., Varghese B. A., 2002, Ap&SS, 281, 751
Szczerba R., Omont A., Volk K., Cox P., Kwok S., 1997, A&A, 317, 859

te Lintel Hekkert P., Versteege-Hansel H. A., Habing H. J., Wiertz M., 1989, A&AS, 78, 399
Ueta T., Meixner M., Bobrowsky M., 2000, ApJ, 528, 861
van der Veen W. E. C. J., Habing H. J., 1988, A&A, 194, 125
Verhoelst T., Waters L. B. F. M., Verhoeff A., Dijkstra C., van Winckel H., Pel J. W., Peletier R. F., 2009, A&A, 503, 837
Vlemmings W. H. T., Amiri N., van Langevelde H. J., Tafoya D., 2014, A&A, 569, A92
Walsh A. J., Breen S. L., Bains I., Vlemmings W. H. T., 2009, MNRAS, 394, L70
Wright E. L. et al., 2010, AJ, 140, 1868
Yamamura I., Makiuti S., Ikeda N., Fukuda Y., Oyabu S., Koga T., White G. J., 2010, AKARI-FIS Bright Source Catalogue Release note Version 1.0. ISAS, Sagamihara
Yung B. H. K., Nakashima J., Imai H., Deguchi S., Diamond P. J., Kwok S., 2011, ApJ, 741, 94
Yung B. H. K., Nakashima J., Imai H., Deguchi S., Henkel C., Kwok S., 2013, ApJ, 769, 20
Yung B. H. K., Nakashima J., Henkel C., 2014, ApJ, 794, 81
Zijlstra A. A., Chapman J. M., te Lintel Hekkert P., Likkel L., Comeron F., Norris R. P., Molster F. J., Cohen R. J., 2001, MNRAS, 322, 280

APPENDIX A: PHOTOMETRIC DATA

The original sets of photometric data used in the current analysis are given in Tables A1–A7.

Table A1. 2MASS photometric data and the $A(V)$ colour excess of each object (see text).

Object	$A(V)$	J band (mag)	σ_J (mag)	H band (mag)	σ_H (mag)	K band (mag)	σ_K (mag)
			Water fountains				
IRAS 15445−5449	0.056	15.693	0.080	12.701	0.040	10.889	0.024
IRAS 15544−5332	44.166	14.265	0.063	12.465	···	11.355	···
IRAS 16342−3814	1.996	11.608	0.033	10.589	0.038	9.569	0.027
IRAS 16552−3050	1.231	16.594	0.181	15.945	0.209	15.125	···
IRAS 18043−2116	35.011	14.546	0.049	13.404	0.062	13.042	0.065
IRAS 18056−1514	4.951	11.334	0.023	10.028	0.023	9.509	0.021
IRAS 18113−2503	3.143	11.630	0.033	10.698	0.034	10.323	0.030
OH 12.8−0.9	18.461	17.041	···	15.725	···	11.639	0.025
IRAS 18286−0959	57.614	15.431	0.097	13.562	0.065	12.674	0.060
OH 16.3−3.0	3.748	11.905	0.024	10.247	0.023	8.904	0.021
W 43A	110.537	16.361	0.126	14.988	0.079	14.120	0.088
IRAS 18455+0448	5.918	15.068	0.056	13.294	0.030	11.305	0.023
IRAS 18460−0151	61.544	13.732	···	13.813	0.057	13.435	0.055
IRAS 18596+0315	11.560	16.501	···	14.945	0.088	14.311	···
IRAS 19134+2131	3.525	16.543	0.128	14.926	0.071	13.464	0.038
IRAS 19190+1102	9.142	16.253	0.118	13.690	···	13.120	···
IRAS 19356+0754	1.017	11.376	0.024	10.770	0.024	10.555	0.021
			AGB stars				
IRAS 14247+0454	0.090	3.091	0.246	2.229	0.266	1.532	0.298
IRAS 18556+0811	7.961	7.162	0.024	5.264	0.026	3.953	0.036
IRAS 19149+1638	8.038	10.107	0.023	7.564	0.031	5.889	0.027
IRAS 19312+1130	1.442	9.044	0.022	7.292	0.055	6.028	0.018
IRAS 19395+1827	4.030	8.049	0.018	6.314	0.026	5.243	0.017
IRAS 19495+0835	0.533	6.487	0.026	4.769	0.034	3.696	0.274
			Post-AGB stars				
IRAS 07134+1005	0.248	6.868	0.021	6.708	0.036	6.606	0.017
IRAS 19024+0044	4.104	12.404	0.026	11.519	0.024	10.763	0.023
IRAS 22272+5435	5.537	5.371	0.020	4.894	0.029	4.508	0.016

Table A2. *WISE* photometric data.

Object	3.4 μm (mag)	$\sigma_{3.4\,\mu m}$ (mag)	4.6 μm (mag)	$\sigma_{4.6\,\mu m}$ (mag)	12 μm (mag)	$\sigma_{12\,\mu m}$ (mag)	22 μm (mag)	$\sigma_{22\,\mu m}$ (mag)
Water fountains								
IRAS 15445−5449	8.883	0.023	7.049	0.019	1.607	0.013	···	···
IRAS 15544−5332	5.889	0.040	3.907	0.054	2.326	0.015	− 0.308	0.016
IRAS 16342−3814	7.701	0.017	6.343	0.015	0.266	0.006	− 3.323	0.001
IRAS 16552−3050	···	···	15.021	0.292	6.697	0.019	5.631	···
IRAS 18043−2116	12.203	0.100	9.382	0.028	3.545	0.015	0.443	0.009
IRAS 18056−1514	7.746	0.023	4.233	0.041	0.599	0.011	− 0.746	0.009
IRAS 18113−2503	10.078	0.025	10.249	0.028	···	···	···	···
OH 12.8−0.9	6.623	0.032	3.854	0.054	0.784	0.020	− 0.806	0.014
IRAS 18286−0959	···	···	3.962	0.044	− 0.441	0.062	− 2.036	0.008
OH 16.3−3.0	5.631	0.063	2.991	0.072	0.160	0.023	− 1.601	0.009
W 43A	13.879	0.347	10.597	0.051	0.451	0.413	− 2.574	0.014
IRAS 18455+0448	7.780	0.025	5.080	0.031	1.306	0.010	− 0.607	0.006
IRAS 18460−0151	11.610	0.052	7.017	0.020	0.824	0.021	− 1.069	0.010
IRAS 18596+0315	11.367	0.030	8.613	0.022	2.696	0.014	− 0.384	0.015
IRAS 19134+2131	11.128	0.023	9.068	0.020	2.107	0.009	− 0.480	0.011
IRAS 19190+1102	12.300	0.261	10.301	0.032	3.717	0.015	− 0.351	0.014
IRAS 19356+0754	6.429	0.046	5.137	0.034	3.349	0.015	− 0.058	0.018
AGB stars								
IRAS 14247+0454	1.287	···	1.300	0.179	− 0.342	0.034	− 2.024	0.001
IRAS 18556+0811	2.683	0.011	1.675	0.378	− 1.102	0.251	− 2.303	0.002
IRAS 19149+1638	3.521	0.130	1.999	0.010	0.450	0.013	− 0.722	0.009
IRAS 19312+1130	4.098	0.094	2.683	0.087	1.135	0.007	0.099	0.015
IRAS 19395+1827	5.034	0.064	3.996	0.022	1.971	0.012	0.639	0.017
IRAS 19495+0835	3.120	0.119	1.789	0.012	− 0.529	0.016	− 1.731	0.006
Post-AGB stars								
IRAS 07134+1005	6.335	0.042	6.198	0.022	− 0.278	0.009	− 2.805	0.002
IRAS 19024+0044	9.945	0.024	8.673	0.020	2.325	0.007	− 1.655	0.010
IRAS 22272+5435	4.845	0.090	3.559	0.048	− 1.054	0.175	− 3.892	0.000

Table A3. *IRAS* photometric data.

Object	12 μm (Jy)	$\sigma_{12\,\mu m}$ (%)	25 μm (Jy)	$\sigma_{25\,\mu m}$ (%)	60 μm (Jy)	$\sigma_{60\,\mu m}$ (%)	100 μm (Jy)	$\sigma_{100\,\mu m}$ (%)
Water fountains								
IRAS 15445−5449	6.88	9	87.20	10	1130.00†	···	2180.00†	···
IRAS 15544−5332	4.64	13	15.50	12	41.50	17	288.00†	···
IRAS 16342−3814	16.20	3	200.00	3	290.00	8	139.00	8
IRAS 16552−3050	2.46	5	10.50	8	9.58	10	17.00†	···
IRAS 18043−2116	6.60†	···	6.76	10	16.60	16	237.00†	···
IRAS 18056−1514	13.60	16	15.20	17	5.94	12	37.80†	···
IRAS 18113−2503	2.90	10	14.80	8	12.90	17	29.20†	···
OH 12.8−0.9	11.60	6	16.90	8	13.90	16	289.00†	···
IRAS 18286−0959	24.90	5	24.50	8	18.40†	···	405.00†	···
OH 16.3−3.0	18.10	8	30.10	13	16.90	18	131.00†	···
W 43A	23.70	4	104.00	5	295.00†	···	2520.00†	···
IRAS 18455+0448	9.35	6	12.60	6	5.47	9	12.60†	···
IRAS 18460−0151	20.90†	···	32.70	8	277.00†	···	291.00	17
IRAS 18596+0315	2.60	9	14.20	8	22.60	11	113.00†	···
IRAS 19134+2131	5.06	4	15.60	5	8.56	9	3.95†	···
IRAS 19190+1102	1.59	7	13.70	6	24.50	16	20.40	15
IRAS 19356+0754	1.12	7	7.99	7	7.62	10	10.90†	···
AGB stars								
IRAS 14247+0454	109.00	10	65.20	7	11.90	9	4.29	12
IRAS 18556+0811	104.00	7	84.70	7	10.20	8	79.90†	···

Table A3 – *Continued.*

Object	12 μm (Jy)	$\sigma_{12\,\mu m}$ (%)	25 μm (Jy)	$\sigma_{25\,\mu m}$ (%)	60 μm (Jy)	$\sigma_{60\,\mu m}$ (%)	100 μm (Jy)	$\sigma_{100\,\mu m}$ (%)
IRAS 19149+1638	14.50	4	14.80	5	3.10	21	13.20†	···
IRAS 19312+1130	9.95	12	7.63	7	1.29	8	2.68†	···
IRAS 19395+1827	8.35	6	6.73	7	1.53	16	21.60†	···
IRAS 19495+0835	80.00	5	65.50	10	11.80	17	3.73	13
				Post-AGB stars				
IRAS 07134+1005	24.50	5	117.00	4	50.10	26	18.70	10
IRAS 19024+0044	2.86	6	48.80	8	42.50	13	15.70†	···
IRAS 22272+5435	73.90	3	302.00	3	96.60	10	41.00†	···

Note. †Upper-band flux limit.

Table A4. *MSX* photometric data.

Object	8.28 μm (Jy)	$\sigma_{8.28\,\mu m}$ (%)	12.13 μm (Jy)	$\sigma_{12.13\,\mu m}$ (%)	14.65 μm (Jy)	$\sigma_{14.65\,\mu m}$ (%)	21.34 μm (Jy)	$\sigma_{21.34\,\mu m}$ (%)
				Water fountains				
IRAS 15445−5449	0.652	4.2	5.389	5.0	13.670	6.1	45.580	6.0
IRAS 15544−5332	2.974	4.1	4.521	5.1	6.735	6.1	8.649	6.1
IRAS 16342−3814	1.540	4.2	13.310	5.0	43.650	6.1	125.600	6.0
IRAS 16552−3050	···	...	···	...	...	...	...	...
IRAS 18043−2116	0.485	4.4	2.287	5.6	4.796	6.1	4.328	6.3
IRAS 18056−1514	10.020	4.1	12.260	5.0	14.140	6.1	10.520	6.1
IRAS 18113−2503	0.691	4.3	2.535	5.7	5.475	6.1	9.635	6.1
OH 12.8−0.9	8.132	4.1	12.340	5.0	18.930	6.1	13.660	6.0
IRAS 18286−0959	29.680	4.1	45.010	5.0	61.540	6.1	33.410	6.0
OH 16.3−3.0	11.860	4.1	20.920	5.0	24.440	6.1	27.080	6.0
W 43A	2.509	4.1	23.870	5.0	53.390	6.1	78.810	6.0
IRAS 18455+0448	5.466	4.1	9.325	5.0	13.440	6.1	11.710	6.1
IRAS 18460−0151	···	...	···	...	...	...	...	...
IRAS 18596+0315	0.484	4.4	2.940	5.4	6.193	6.1	9.310	6.1
IRAS 19134+2131	1.224	4.2	5.058	5.3	8.853	6.1	10.090	6.1
IRAS 19190+1102	0.120◇	8.0	1.175◇	7.9	3.450	6.3	8.092	6.1
IRAS 19356+0754	···	...	···	...	...	...	...	...
				AGB stars				
IRAS 14247+0454	···	...	···	...	...	...	...	...
IRAS 18556+0811	72.930	4.1	86.550	5.0	65.560	6.1	72.790	6.0
IRAS 19149+1638	24.130	4.1	26.920	5.0	20.180	6.1	22.040	6.0
IRAS 19312+1130	9.494	4.1	9.701	5.0	7.005	6.1	7.889	6.1
IRAS 19395+1827	4.098	4.1	4.971	5.2	3.641	6.3	···	···
IRAS 19495+0835	···	...	···	...	...	...	...	...
				Post-AGB stars				
IRAS 07134+1005	···	...	···	...	...	...	...	...
IRAS 19024+0044	0.679	4.3	2.618	5.6	8.407	6.1	32.610	6.0
IRAS 22272+5435	25.070	4.1	87.850	5.0	95.380	6.1	186.600	6.0

Note. ◇Unreliable flux value.

Table A5. *AKARI* photometric data.

Object	9 μm (Jy)	$\sigma_{9\,\mu m}$ (Jy)	18 μm (Jy)	$\sigma_{18\,\mu m}$ (Jy)	65 μm (Jy)	$\sigma_{65\,\mu m}$ (Jy)	90 μm (Jy)	$\sigma_{90\,\mu m}$ (Jy)	140 μm (Jy)	$\sigma_{140\,\mu m}$ (Jy)	160 μm (Jy)	$\sigma_{160\,\mu m}$ (Jy)
Water Fountains												
IRAS 15445−5449	0.655	0.01	28.080	0.07	...	...	...	...	...	...	...	...
IRAS 15544−5332	2.824	0.04	7.315	0.03	...	...	...	...	...	...	...	...
IRAS 16342−3814	1.776	0.03	89.450	2.09	...	...	...	...	...	...	...	...
IRAS 16552−3050	0.315	0.04	5.555	0.15	10.150	1.01	7.897	0.53	4.157	1.36	...	...
IRAS 18043−2116	0.316	0.02	4.347	0.04	11.210	3.46	9.279	1.19	...	...	...	...
IRAS 18056−1514	10.310	0.06	15.280	0.09	6.283	2.07	4.518	0.87	...	...	...	...
IRAS 18113−2503	...	...	6.715	0.05	16.190	5.25	14.930	2.36	...	...	...	...
OH 12.8−0.9	8.223	0.07	15.740	0.05	...	...	13.010$^{\diamond}$	2.64	...	...	...	...
IRAS 18286−0959	21.980	0.39	45.840	0.19	51.580	4.57	25.830	3.49	...	...	...	...
OH 16.3−3.0	13.090	0.79	28.150	0.97	15.920	1.49	12.750	0.50	8.112	3.35	...	...
W 43A	2.191	0.14	...	...	...	...	...	...	...	...	...	...
IRAS 18455+0448	4.889	0.02	12.620	0.09	5.627	0.34	4.771	0.16	...	...	...	...
IRAS 18460−0151	...	...	...	...	...	...	...	...	...	...	...	...
IRAS 18596+0315	0.598	0.02	7.817	0.08	...	...	...	...	...	...	...	...
IRAS 19134+2131	1.116	0.01	9.708	0.15	7.776	0.61	6.266	0.65	3.396	0.79	...	...
IRAS 19190+1102	0.133	0.01	6.100	0.05	17.670	3.82	12.900	2.45	...	...	...	...
IRAS 19356+0754	...	...	...	...	...	...	...	...	...	...	...	...
AGB stars												
IRAS 14247+0454	111.500	20.00	80.670	0.27	9.944	0.58	7.189	0.24	...	...	...	...
IRAS 18556+0811	94.540	0.81	64.970	14.30	...	...	...	...	...	...	...	...
IRAS 19149+1638	25.910	0.01	16.310	0.03	...	...	...	...	...	...	...	...
IRAS 19312+1130	8.348	3.19	6.724	1.24	...	...	0.504	0.08	...	...	...	...
IRAS 19395+1827	7.761	1.77	7.281	1.06	...	...	1.002	0.20	...	...	...	...
IRAS 19495+0835	57.070	14.40	43.540	14.70	7.072	0.87	4.724	0.69	...	...	...	...
Post-AGB stars												
IRAS 07134+1005	8.909	0.06	66.250	1.15	51.260	2.64	26.750	1.95	8.701	1.19	...	...
IRAS 19024+0044	0.814	0.01	21.980	0.11	...	...	...	...	6.178	0.59	...	...
IRAS 22272+5435	31.000	0.21	148.800	1.32	83.770	1.85	36.870	3.08	14.830	2.28	8.472	1.85

Note. $^{\diamond}$Unreliable flux value.

Table A6. IRAC and MIPS (24-μm) photometric data. The values are obtained by performing photometry on corresponding images, if applicable. Hence the data here are presented directly in terms of W m^{-2}.

Object	3.6 μm	$\sigma_{3.6\,\mu m}$	4.5 μm	$\sigma_{4.5\,\mu m}$	5.8 μm	$\sigma_{5.8\,\mu m}$	8.0 μm	$\sigma_{8.0\,\mu m}$	24 μm	$\sigma_{24\,\mu m}$
					(10^{-13} W m^{-2})					
Water fountains										
IRAS 15445−5449	0.84	0.03	1.42	0.07	1.21	0.09	1.52	0.08	28.38‡	...
IRAS 15544−5332	8.33	0.84	10.88	0.34	2.01	0.22	10.81	0.18	8.87‡	...
IRAS 16342−3814	...	...	...	...	...	...	...	...	...	...
IRAS 16552−3050	...	...	...	...	...	...	...	...	...	...
IRAS 18043−2116	0.05	0.01	0.21	0.02	0.61	0.09	1.61	0.11	6.83	0.19
IRAS 18056−1514	...	...	...	...	...	...	...	...	...	...
IRAS 18113−2503	...	...	...	...	...	...	...	...	...	...
OH 12.8−0.9	6.22	0.23	10.86	0.28	39.87	0.90	29.42	0.89	12.33‡	...
IRAS 18286−0959	...	...	13.41	0.69	72.06	1.12	38.06	1.40	23.90‡	...
OH 16.3−3.0	...	...	...	...	...	...	...	...	...	...
W 43A	0.07	0.01	0.08	0.01	1.27	0.04	9.54	0.44	135.20	26.00
IRAS 18455+0448	...	...	...	...	...	...	...	...	...	...
IRAS 18460−0151	0.20	0.01	2.35	0.22	13.99	0.33	19.29	0.11	20.04‡	...
IRAS 18596+0315	0.09	0.01	0.31	0.02	1.10	0.05	2.84	0.07	10.21‡	...
IRAS 19134+2131	...	...	...	...	...	...	...	...	...	...
IRAS 19190+1102	...	...	...	...	...	...	...	...	...	...
IRAS 19356+0754	...	...	...	...	...	...	...	...	...	...
AGB stars										
IRAS 14247+0454	...	...	...	...	...	...	...	...	...	...
IRAS 18556+0811	...	...	...	...	...	...	...	...	...	...

Table A6 – *Continued.*

Object	3.6 μm	$\sigma_{3.6\,\mu m}$	4.5 μm	$\sigma_{4.5\,\mu m}$	5.8 μm	$\sigma_{5.8\,\mu m}$	8.0 μm	$\sigma_{8.0\,\mu m}$	24 μm	$\sigma_{24\,\mu m}$
					(10^{-13} W m^{-2})					
IRAS 19149+1638	...	...	...	...	...	...	...	...	...	...
IRAS 19312+1130	...	...	...	...	...	...	...	...	...	...
IRAS 19395+1827	...	...	...	...	...	...	...	...	...	...
IRAS 19495+0835	...	...	...	...	...	...	...	...	...	...
					Post-AGB stars					
IRAS 07134+1005	...	...	...	...	...	...	...	...	...	...
IRAS 19024+0044	...	...	...	...	...	...	...	...	50.23	0.44
IRAS 22272+5435	...	...	...	...	...	...	...	...	...	...

Note. ‡Lower band flux limit.

Table A7. NMA and JVLA data for W43A.

Frequency (GHz)	Flux (mJy)	$\sigma_{\rm Flux}$ (mJy)	rms (mJy)	Beam size
		NMA		
98.20	24.69	4.84	1.72	$3.8'' \times 3.3''$
110.20	31.94	5.14	2.82	$3.9'' \times 2.9''$
134.45	70.68	23.10	11.02	$3.6'' \times 2.2''$
146.45	108.70	33.00	10.51	$2.8'' \times 1.8''$
		JVLA		
10.10	0.49†	...	0.16	$4.48'' \times 3.33''$
24.20	0.24	0.06	0.03	$1.14'' \times 0.93''$
46.00	1.34	0.08	0.04	$0.54'' \times 0.46''$

Note. †3σ upper flux limit.

This paper has been typeset from a TEX/LATEX file prepared by the author.